Available online at www.sciencedirect.com
SCIENCE DIRECT®
International Journal of Solids and Structures 42 (2005) 2929–2948
INTERNATIONAL JOURNAL OF SOLIDS and STRUCTURES
www.elsevier.com/locate/ijsolstr

Numerical prediction of fracture in the Taylor test

X. Teng [a,*], T. Wierzbicki [a,*], S. Hiermaier [b], I. Rohr [b]

[a] *Impact and Crashworthiness Lab, Room 5-218, Ocean Engineering Department, Massachusetts Institute of Technology, 77 Mass Avenue, Cambridge, MA 02139, USA*
[b] *Ernst Mach Institute, Eckerstrasse 4, D-79104 Freiburg, Germany*

Received 27 February 2004; received in revised form 24 September 2004
Available online 5 November 2004

Abstract

A flat-nosed cylinder moving at a sufficiently high impact velocity in the classical Taylor test will always fracture. In this paper, fracture phenomena and fracture mechanisms in the Taylor test are investigated numerically based on a recently developed ductile fracture locus with the cut-off value for the negative stress triaxiality at $-1/3$. The impact velocity of the projectile ranges from 240 m/s to 600 m/s. The lower velocity is applied to a less ductile 2024-T351 aluminum alloy cylinder while the higher velocity is introduced for more ductile Weldox 460 E steel. Three distinct fracture modes are recreated numerically: the confined fracture inside the cylinder, the shear cracking on the lateral surface, and the petalling, all of which are consistent with experimental results presented in the open literature. It is found that a more ductile cylinder tends to fail by petalling while a less ductile one by shear cracking. Confined fracture is a common failure mode for both materials, which occurs in a wide range of the impact velocity. The ductile fracture criterion with the cut-off value predicts realistic fracture patterns for short cylinders deforming predominantly under compression.
© 2004 Elsevier Ltd. All rights reserved.

Keywords: Taylor test; Ductile fracture criterion; Petalling; Shear cracking; Confined fracture

1. Introduction

The Taylor test in which a deformable flat-nosed cylinder is fired against a fixed, rigid wall was originally proposed to determine dynamic yield stresses of materials (Taylor, 1948). As large plastic deformation, high strain rates, and elevated temperature are involved, the Taylor test is also widely used to verify material

* Corresponding authors. Tel.: +1 617 253 6055; fax: +1 617 253 1962 (X. Teng), tel.: +1 617 253 2104; fax: +1 617 253 1962 (T. Wierzbicki).
E-mail addresses: xteng@mit.edu (X. Teng), wierz@mit.edu (T. Wierzbicki).

0020-7683/$ - see front matter © 2004 Elsevier Ltd. All rights reserved.
doi:10.1016/j.ijsolstr.2004.09.039

constitutive models by comparing numerical prediction with experimental response, e.g. Johnson and Holmquist (1988), and Rohr et al. (2003). A careful literature review reveals that over 400 papers relating to the Taylor test have been published over the past 50 years (Walley, 2003). Most of the papers focus on dynamic yield stresses and material constitutive models, but only few authors investigated fracture phenomena and fracture mechanisms in the Taylor test. Cracks or fragments will be generated in the Taylor test if a cylinder is fired at a sufficiently high impact velocity. Couque (1998) observed several spiral cracks formed on the lateral surface of the cylinder in symmetric Taylor tests on swaged tungsten alloys. Woodward et al. (1992) presented several pictures illustrating tensile splitting as well as fragmentation in steel specimens. Grady and Kipp (1989) found from sectioned post-test specimens that a number of voids nucleate, grow, and coalesce in the region near the impact interface and the central axis. Worswick and Pick (1995), and Addessio et al. (1993) used the Gurson material model (Gurson, 1975) to simulate the process of void growth.

Compared with a great number of experimental studies and numerical simulations of the process of mushrooming deformation, numerical prediction of fracture in the Taylor test appears to be lacking in the literature. In fact, numerical prediction of crack growth in a three-dimensional body under multi-axial dynamic loading is still a challenging problem. The accuracy of numerical simulations of fracture would depend on a chosen criterion for initiation and propagation of cracks. Because several distinct fracture modes may occur separately or simultaneously in specimens, the applicability of a specific ductile fracture criterion can be examined by performing the Taylor test and parallel numerical simulations. In particular, the Taylor test can be used to investigate effects of negative hydrostatic stress on fracture mechanisms and failure modes, since the cylinder is predominantly under compression during the impact process. Most ductile fracture criteria involving the effective plastic strain and the stress triaxiality were developed on basis of a series of tensile tests on smooth and notched axisymmetric specimens. Therefore, they cover just the range of the stress triaxiality higher than 1/3. In practical application, several authors extrapolated these fracture loci to the range of the negative stress triaxiality (Johnson and Cook, 1985; Børvik et al., 2001b). Such as extension may be questionable.

The objective of the present paper is to formulate and solve the classical Taylor problem, which is dominated by compression for which ductile fracture could not be easily predicted. Detailed numerical simulation is performed using the newly developed ductile fracture locus by Bao and Wierzbicki (2004). A cut-off value for the negative stress triaxiality at $\sigma_h/\bar{\sigma} = -1/3$ was introduced in this fracture locus. The initial impact velocity of the cylinder ranges from 240 m/s to 600 m/s. The lower velocity is applied to 2024-T351 aluminum alloy, while the higher velocity is introduced for Weldox 460 E steel, which is more ductile than 2024-T351 aluminum alloy. Three distinct fracture macro-modes are identified: confined fracture inside the specimen, petalling, and shear cracking. Corresponding fracture mechanisms are discussed. The effect of the cut-off value on the failure process is also studied.

2. Finite element modeling

2.1. Computational model

Consider normal impact of a flat-nosed cylindrical projectile onto a rigid wall (see Fig. 1). The cylindrical projectile is of the diameter $d = 6$ mm and the length $l = 30$ mm. The friction coefficient between the front surface of the projectile and the rigid wall is assumed to be $\mu = 0.1$. ABAQUS/Explicit was used to simulate the deformation and fracture process of the cylinder.

As observed from the retrieved specimens (Woodward et al., 1992), either tensile splitting or spiral cracking develops on the lateral surface of the projectile. Hence, a 3-D solid finite element model was built rather than an axisymmetric model (see Fig. 2). Eight-node, linear brick elements with reduced integration

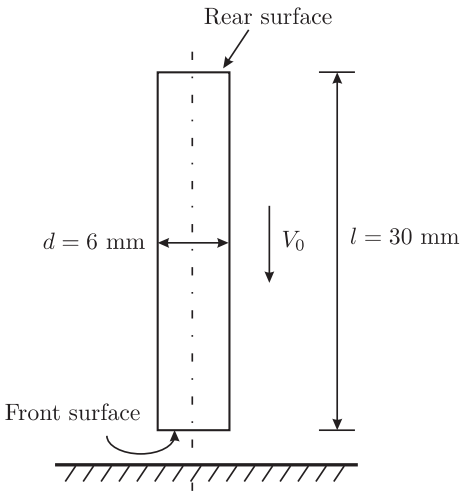

Fig. 1. Schematic representation of a cylindrical projectile impacting a rigid wall.

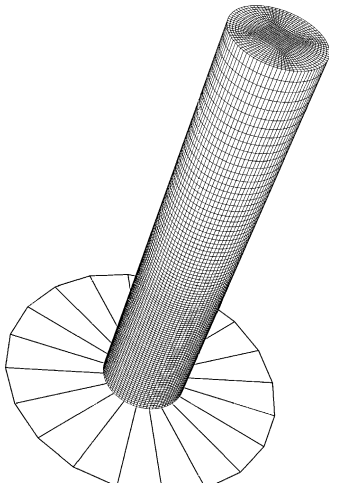

Fig. 2. Finite element model of the projectile-target system.

(C3D8R) were used. Very fine meshes were generated in the front part where fracture was expected to occur, while relatively coarse meshes were used in the rear part of the cylinder. Totally there are 120,000 elements in the FE model. The minimum element size is approximately $0.2\,\text{mm} \times 0.2\,\text{mm} \times 0.2\,\text{mm}$. The technique of element deletion embedded in ABAQUS/Explicit is used to model crack initiation and propagation. In reality, a crack is formed due to separation of materials. Hence, the size of elements must be sufficiently small to attenuate effects of element removal on the impact response. The rigid wall was modeled as a rigid circular surface. The kinematic contact constraint was prescribed at the impact interface, which allows the projectile to elastically rebound from the rigid wall at the end of the impact process.

2.2. Material constitutive model

Due to simplicity and availability of material coefficients, the Johnson–Cook (JC) material model implemented in ABAQUS/Explicit was used in the present calculation. The material model should not be confused with the fracture model that will be discussed later. In the JC model the equivalent stress, $\bar{\sigma}$, is an explicit function of the equivalent plastic strain, $\bar{\varepsilon}_{\mathrm{pl}}$, the temperature, T, and the plastic strain rate, $\dot{\bar{\varepsilon}}_{\mathrm{pl}}$ (Johnson and Cook, 1983):

$$\bar{\sigma} = [A + B\bar{\varepsilon}_{\mathrm{pl}}^{n}]\left[1 + C\ln\left(\frac{\dot{\bar{\varepsilon}}_{\mathrm{pl}}}{\dot{\bar{\varepsilon}}_0}\right)\right]\left[1 - \left(\frac{T - T_0}{T_{\mathrm{m}} - T_0}\right)^{q}\right], \tag{1}$$

where $\dot{\bar{\varepsilon}}_0$ is the reference plastic strain rate, T_0 and T_{m} are the room temperature and the material melting temperature, respectively, and A, B, n, C, and q are five material constants. The JC model accounts for isotropic strain hardening, strain rate sensitivity, and thermal softening in the uncoupled form. The first term of the right hand side of Eq. (1) represents the quasi-static stress–strain relation at room temperature; the second term signifies the strain-rate hardening; the third term means the temperature dependence of the stress–strain relation. It should be pointed out that in the computation, the material behaves elastically up to the point of initial yield and then follows Eq. (1).

The high velocity impact process is usually assumed to be adiabatic, because heat generated by plastic work in the localized region does not have sufficient time to be conducted to the surrounding material. The increase in local temperature T owing to plastic work is given by

$$T = \int \frac{\alpha}{\rho c_p}\sigma^{ij}\,\mathrm{d}\varepsilon_{\mathrm{pl}}^{ij}, \quad i,j = 1,2,3, \tag{2}$$

where ρ is the material density, c_p is the specific heat, σ^{ij} and $\varepsilon_{\mathrm{pl}}^{ij}$ are the components of the stress and plastic strain tensors, respectively, and α is the fraction of plastic work converted to heat. It is generally accepted that $\alpha \cong 0.9$ (Bai and Dodd, 1992).

Two types of materials: 2024-T351 aluminum alloy and Weldox 406 E steel, are considered in the present paper, which represent a less and a more ductile metal, respectively. The material constants in the JC model for both materials are listed in Tables 1 and 2, where σ_0 is the plastic flow stress; $c = \sqrt{\sigma_0/\rho}$ is the transverse plastic stress wave speed; $D_1, \ldots, D_5$ are five material constants in the JC fracture criterion. Detailed discussion on the determination of the material coefficients for 2024-T351 aluminum alloy was presented by Teng and Wierzbicki (2004). Mechanical properties of Weldox 406 E steel were taken from Børvik et al. (2001a). It should be pointed out that two sets of the material constants in the JC constitutive model were calibrated by Børvik et al. (2001a) for Weldox 460 E steel: one set corresponds to the case that damage softening was taken into account in the material model, the other applies to the case where the material model is uncoupled to the fracture model. In the present paper, the latter set is used. As shown in Figs. 3 and 4, the stress–strain relationships of both 2024-T351 aluminum alloy and Weldox 406 E steel are much more sensitive to temperature than to the strain rate.

Table 1
Material constants for 2024-T351 aluminum alloy

E (GPa)	ν	ρ (kg/m^3)	$\dot{\bar{\varepsilon}}_0$ (s^{-1})	C	c_p (J/kgK)	α	T_{m} (K)	T_0 (K)	q
74.66	0.3	2700	3.33×10^{-4}	0.0083	875	0.9	775	293	1.0
A (MPa)	B (MPa)	n	σ_0 (MPa)	c (m/s)	D_1	D_2	D_3	D_4	D_5
352	440	0.42	565.5	457.6	0.13	0.13	−1.5	0.011	0.0

Table 2
Material constants for Weldox 460 E steel

E (GPa)	v	ρ (kg/m^3)	$\dot{\bar{\varepsilon}}_0$ (s^{-1})	C	c_p (J/kgK)	α	T_m (K)	T_0 (K)	q
200	0.33	7850	5.00×10^{-4}	0.0123	452	0.9	1800	293	0.94
A (MPa)	B (MPa)	n	σ_0 (MPa)	c (m/s)	D_1	D_2	D_3	D_4	D_5
490	383	0.45	808.6	321.0	0.0705	1.732	−0.54	0.015	0.0

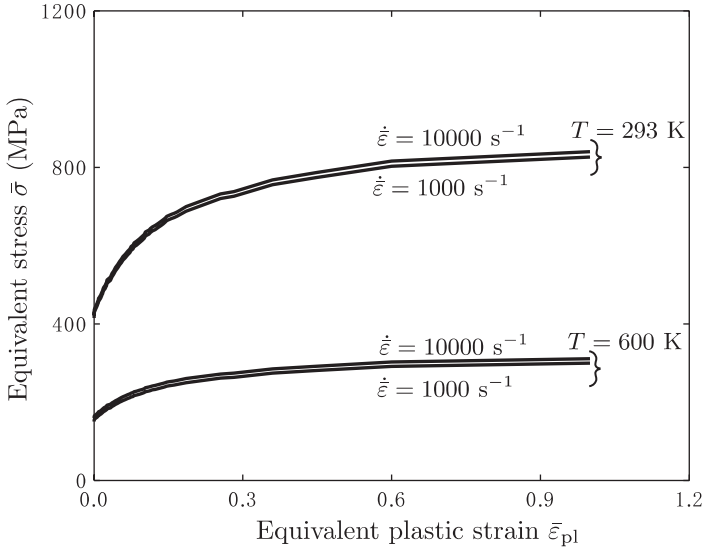

Fig. 3. Equivalent stress versus plastic strain under various strain rates and temperature for 2024-T351 aluminum alloy using Eq. (1).

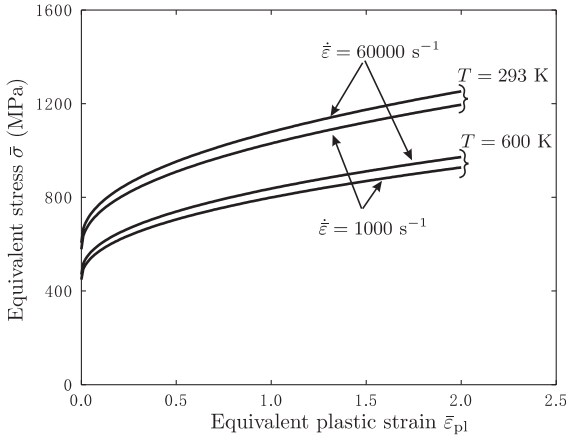

Fig. 4. Equivalent stress versus plastic strain under various strain rates and temperature for Weldox 460 E steel using Eq. (1).

2.3. Ductile fracture criteria

A fracture criterion has to be assigned to predict crack formation in the projectile. The cylinder in the Taylor test usually does not have any macro-cracks before experiments. The front part of the cylinder undergoes large plastic deformation before crack formation and growth. The plastic deformed region is so large that it is beyond the requirement for K-dominance or J-dominance. Hence, the widely used dynamic stress intensity factors or J-integrals as fracture criteria are not applicable to the Taylor test. At the same time, a ductile fracture criterion formulated in terms of the effective plastic strain and the stress triaxiality was shown to be applicable to the problem of high velocity impact (Teng and Wierzbicki, 2004).

In ABAQUS/Explicit, the cumulative damage D at a material point is defined as an integral with respect to the effective plastic strain:

$$D = \int_0^{\bar{\varepsilon}_{\mathrm{pl}}} \frac{\mathrm{d}\bar{\varepsilon}_{\mathrm{pl}}}{\bar{\varepsilon}_{\mathrm{f}}\left(\frac{\sigma_h}{\bar{\sigma}}, \dot{\bar{\varepsilon}}_{\mathrm{pl}}, T\right)}, \tag{3}$$

where $\bar{\varepsilon}_{\mathrm{f}}$ is the fracture strain as a function of the stress triaxiality, strain rate, and temperature. When the cumulative damage D exceeds unity at an integration point of an element, all the deviatoric stress components are suddenly set to zero at this point. The whole element is considered to fail if the accumulated damage at all the integration points exceeds the critical value. ABAQUS/Explicit provides two options to treat the failed elements. Either the failed elements completely lose their load carrying ability, or the failed elements are still capable of transmitting pressure but neither tension nor shear. If the former option is used, the failed elements will no longer participate in the calculation. The time step required for the computational stability will not be determined from these severely distorted elements. Hence, the calculation using the former option is much faster than using the latter one. The latter option is activated in all calculations presented in Section 3.

In the presentation of the results the failed elements are removed to illustrate crack initiation and growth in ABAQUS/Explicit. In reality, cracks are formed as the originally coherent material is separated. The technique of element deletion is effective in some 2-D cases, for example, through-thickness crack propagation in shear plugging and tensile tearing as shown by Børvik et al. (2002); Teng and Wierzbicki (2004). However, this technique should be used with care in 3-D cases such as the Taylor test, since a failed region may be large and cracks formed may close later on due to the predominant compression.

The effects of strain rates and temperature on the fracture strain are much smaller than that of the stress triaxiality for 2024-T351 aluminum alloy (Johnson and Cook, 1985) and Weldox E 460 steel (Børvik et al., 2001b, 2003; Hopperstad et al., 2003), as represented by the fracture coefficients in Tables 1 and 2. As a first approximation, the fracture strain is assumed to be a function only of the stress triaxiality. Both effects of the strain rate and temperature on the damage accumulation are taken into account in an indirect way through the calculation of the stress.

Several relationships between the fracture strain and the stress triaxiality were proposed in the literature, e.g. McClintock (1968), and Rice and Tracey (1969). Recently, a new fracture locus that consists of three branches was developed by Bao and Wierzbicki (2004) for 2024-T351 aluminum alloy, which covers a wide range of the stress triaxiality,

$$\bar{\varepsilon}_f = \begin{cases} \infty & \frac{\sigma_h}{\bar{\sigma}} \leqslant -\frac{1}{3} \\ 0.1225\left(\frac{\sigma_h}{\bar{\sigma}} + \frac{1}{3}\right)^{-0.46} & -\frac{1}{3} < \frac{\sigma_h}{\bar{\sigma}} < 0 \\ 1.9\left(\frac{\sigma_h}{\bar{\sigma}}\right)^2 - 0.18\frac{\sigma_h}{\bar{\sigma}} + 0.21 & 0 < \frac{\sigma_h}{\bar{\sigma}} < 0.4 \\ \exp\left(-1.944\frac{\sigma_h}{\bar{\sigma}}\right) & 0.4 < \frac{\sigma_h}{\bar{\sigma}} \end{cases}, \tag{4}$$

The unique feature of the present fracture locus is that if the current stress triaxiality is lower than $-1/3$, the increase in the effective plastic strain does not contribute to the damage accumulation. Another ductile fracture criterion proposed by Johnson and Cook (1985) is of the form:

$$\bar{\varepsilon}_{\mathrm{f}} = D_1 + D_2 \exp\left(D_3 \frac{\sigma_{\mathrm{h}}}{\bar{\sigma}}\right), \tag{5}$$

where the values of three constants: D_1, D_2, and D_3, are listed in Tables 1 and 2, respectively, for 2024-T351 aluminum alloy and Weldox 460 E steel. Comparison between the BW's and JC's fracture loci for 2024-T351 aluminum alloy is shown in Fig. 5. A more detailed discussion on the fracture locus for 2024-T351 aluminum alloy was presented by Teng and Wierzbicki (2004) and Bao et al. (in press).

Hopperstad et al. (2003) and Børvik et al. (2003) performed a series of tensile tests on smooth and notched axisymmetric Weldox 460 E steel specimens and parallel numerical simulations, which gives the fracture strain in the range of stress triaxiality only from 1/3 up. Since neither shear nor compression tests were conducted, fracture properties in the range of low stress triaxialities were not available. The fracture strain at pure shear ($\sigma_{\mathrm{h}}/\bar{\sigma} = 0$) was estimated from an analytical model (Børvik et al., 2001b). By curve-fitting the tensile test points and the estimated torsion point, the fracture locus given by the exponential function of the stress triaxiality was determined for Weldox 460 E steel. The three fracture coefficients are listed in Table 2. This fracture locus was extrapolated to the range of the negative stress triaxiality in practical application. The present authors think that the concept of extrapolation is questionable. Teng and Wierzbicki (2004) showed this type of fracture criterion was unable to give realistic results in the problem of rigid mass-to-beam/plate impact while the fracture loci with the cut-off value for the negative stress triaxiality successfully captured the failure process. Considering this fact, a modified fracture locus with the cut-off value for the stress triaxiality at $\sigma_{\mathrm{h}}/\bar{\sigma} = -1/3$ is introduced, which is the same as the original one calibrated by Børvik et al. (2001b) in the range of $\sigma_{\mathrm{h}}/\bar{\sigma} > -1/3$ (see Fig. 6).

The fracture criterion with the cut-off value for the stress triaxiality is defined in all the calculations presented in Section 3. Comparison of the failure process between both fracture loci with and without the cut-off value will be addressed in Section 4.

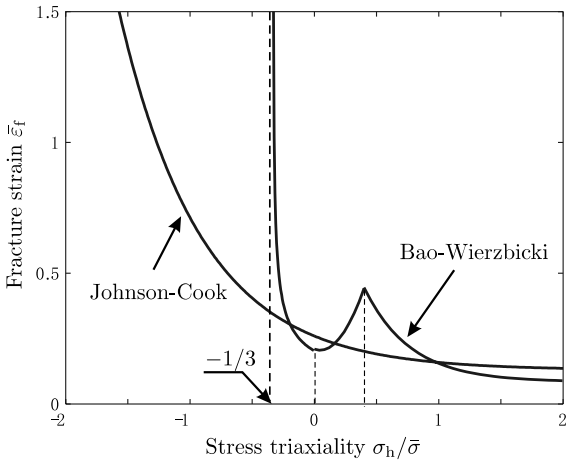

Fig. 5. Fracture loci for 2024-T351 aluminum alloy.

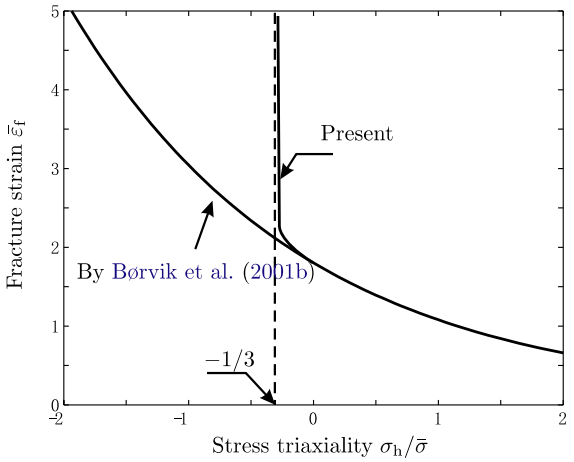

Fig. 6. Fracture loci for Weldox 460 E steel.

3. Fracture mechanisms

3.1. Mushrooming deformation

Immediately upon impact, elastic waves followed by plastic waves are generated at the impact interface, and travel back and forth between the front and rear surfaces. The cylinder gradually slows down, and finally rebounds from the rigid wall as the stored elastic energy is released. The front part of the cylinder bulges out due to compression while the rear part keeps almost undeformed. This deformation process of the cylinder illustrated in Fig. 7 shows a familiar mushroom-like deformation mode in the Taylor test. There is an extensive literature on this subject where comparison are made between the experimentally measured and numerically predicted mushrooming profiles, specimen shortening, and time history of the velocity of the rear surface. Our plasticity model is consistent with previous findings but does not bring any new features. What is entirely new is the prediction of fracture that will be dealt with in the remaining of the paper.

3.2. Confined fracture

At a relatively low impact velocity, a number of voids or even cracks may be generated inside specimens although no cracks are observed on the exterior surface. This type of failure relating to void nucleation, growth, and coalescence has been demonstrated experimentally by, e.g. Worswick and Pick (1995), and Addessio et al. (1993), and also numerically using the Gurson material model. In the present paper this failure mode is successfully recreated using the conventional plasticity model combined with a suitable ductile fracture criterion. As shown in Fig. 8, several elements fail in the region near the front surface and the symmetry axis. Since the failed elements are confined by the rigid wall and the surrounding intact materials, this type of failure in the Taylor test is term "confined fracture" here.

A typical point located at the symmetry axis is selected to illustrate the loading history of the failed region (see Fig. 9). Immediately upon impact, compressive stress waves are generated in both axial and radial directions. At about $t = 0.76\,\mu s$ a radial unloading stress wave of extremely high amplitude arrives at the

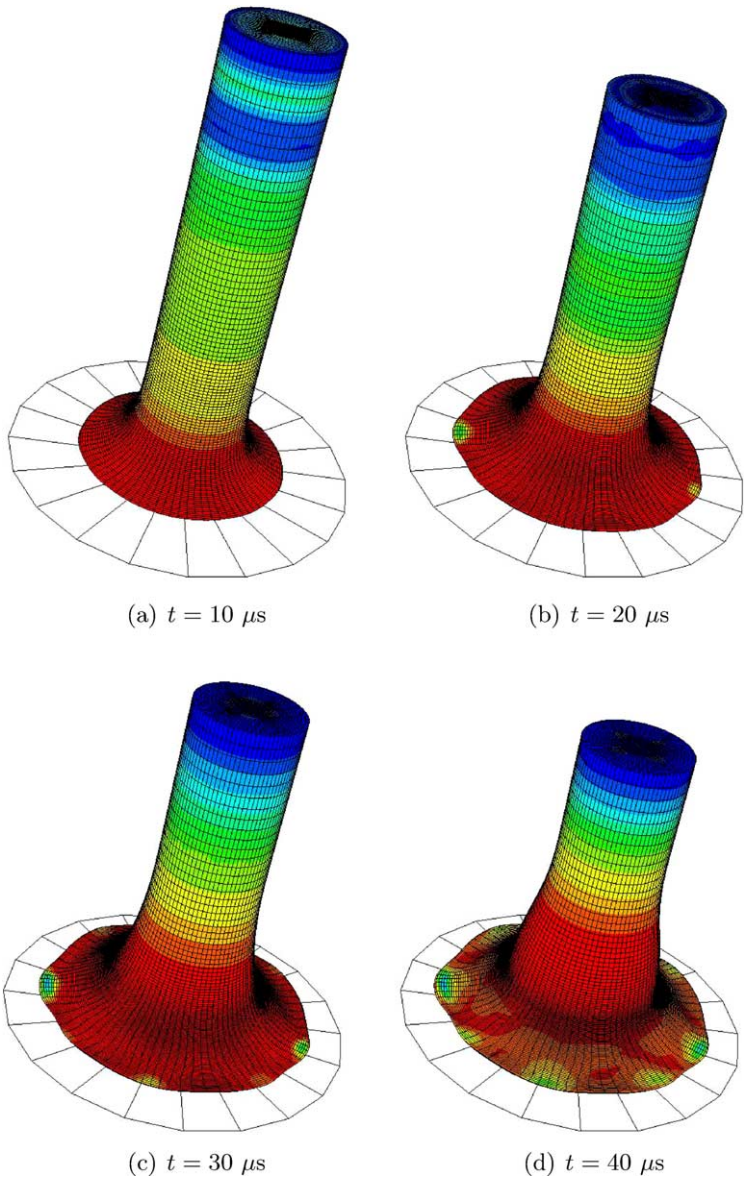

Fig. 7. Mushrooming deformation process of the Weldox 460 E steel projectile at $V_0 = 400\,\mathrm{m/s}$.

symmetry axis. As the radial stress waves travel back and forth from the symmetry axis to the free lateral surface, all three stress components of the stress tensor $(\sigma_r, \sigma_\theta, \sigma_z)$ oscillate with time. The average period is about 1.87 μs.

Fig. 10 shows the history of the axial displacement of the central point of the front surface. Contrary to intuition, the central part of the front surface does not always stay at a close contact with the rigid wall. Immediately after impact a small gap between the front surface and the rigid wall is temporarily formed, which closes after about $t = 4\,\mu s$ until the whole projectile elastically rebounds from the rigid wall. This

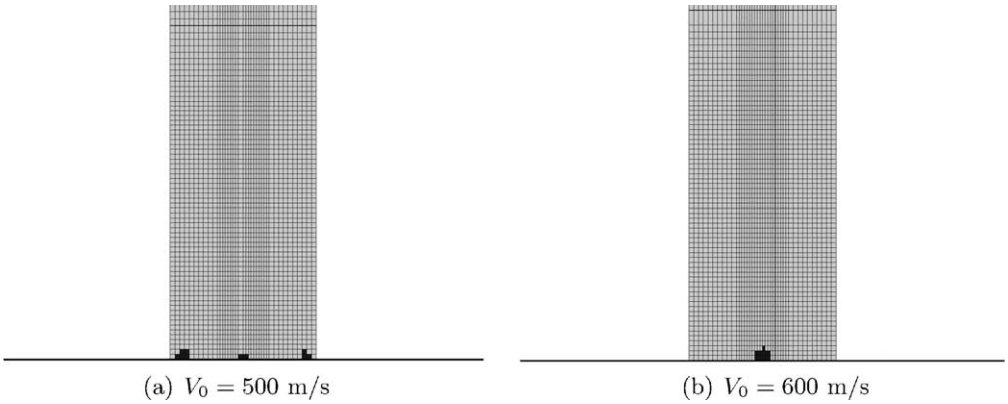

Fig. 8. Confined fracture: failed regions represented by dark elements in an axial section of the Weldox 460 E steel projectile. Failed elements in this figure were brought back to the initial, undeformed configuration.

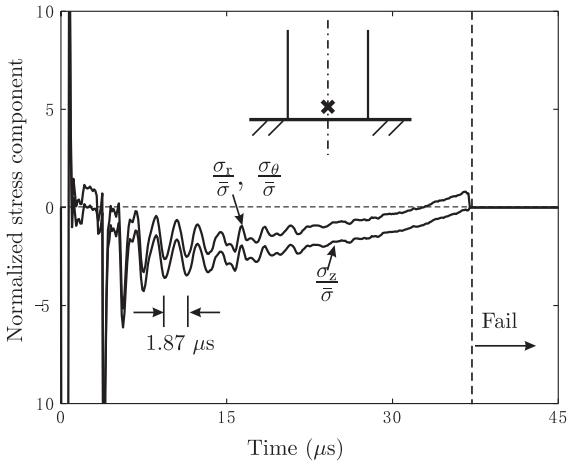

Fig. 9. History of the normalized stress components at a point in the symmetry axis of the projectile. The point is 0.6 mm away from the front surface.

finding is consistent with the numerical results by Worswick and Pick (1995) and Addessio et al. (1993) using the Gurson material model.

The first several stress waves are mainly responsible for void nucleation and coalescence inside the specimen (see Fig. 11). As the gap closes, the compression becomes dominant in the central part of the cylinder, i.e. the stress triaxiality is lower than $-1/3$. Hence, the void growth takes place mainly in the initial phase of the impact process and is suppressed later on.

The size of the failed region inside the specimen increases with the impact velocity (see Fig. 8). In the case with a relatively low impact velocity, nucleated and coalesced voids or cracks may be still observed from sectioned post-test specimens. However, at a much higher velocity, the voids and cracks generated in the initial phase of the impact process could disappear or are difficult to discern due to subsequent crush by the surrounding materials.

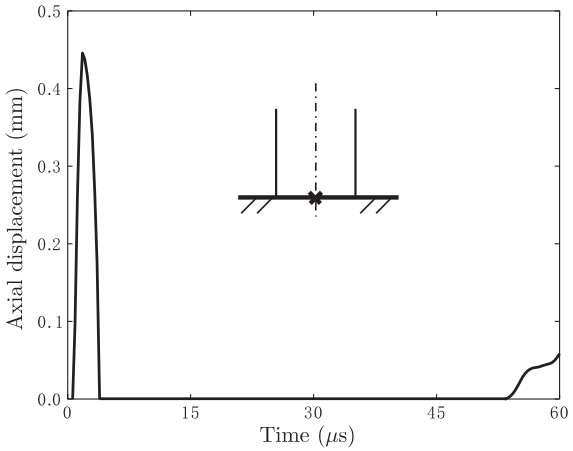

Fig. 10. History of the axial displacement of the central point of the front surface.

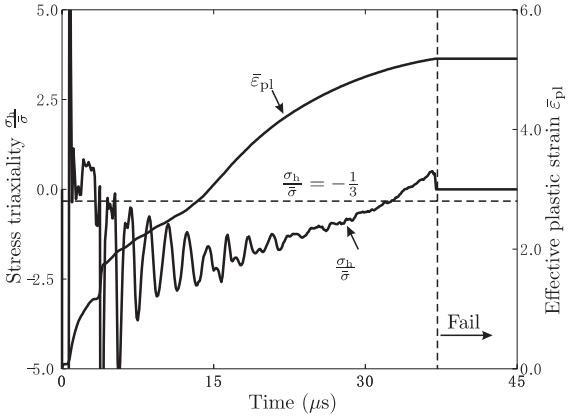

Fig. 11. History of the plastic strain and the stress triaxiality at a point at the symmetric axis of the projectile. The point is 0.6 mm away from the front surface.

3.3. Petalling

As the initial impact velocity increases further to $V_0 = 600\,\text{m/s}$, another fracture mode: petalling, is predicted in the Weldox 460 E steel cylinder. The process of deformation and fracture of the projectile is shown in Fig. 12. Different from the preceding cases with low impact velocities, a number of small cracks are generated on the front surface due to radial stress wave at $V_0 = 600\,\text{m/s}$. However, only four major cracks survive and propagate radially toward the symmetry axis due to tensile hoop stresses. As the velocity of the rear part of the cylinder decreases, these cracks are finally arrested.

The failed elements are removed to show crack initiation and growth in Fig. 12. In reality, the crack formation is due to separation of materials microscopically and macroscopically. Therefore, the crack openings illustrated in Fig. 12 may be a little larger than real ones.

To provide an insight into the failure mechanism of petalling, a point located at the periphery of the front surface is chosen to demonstrate the history of the stress triaxiality and the effective plastic strain.

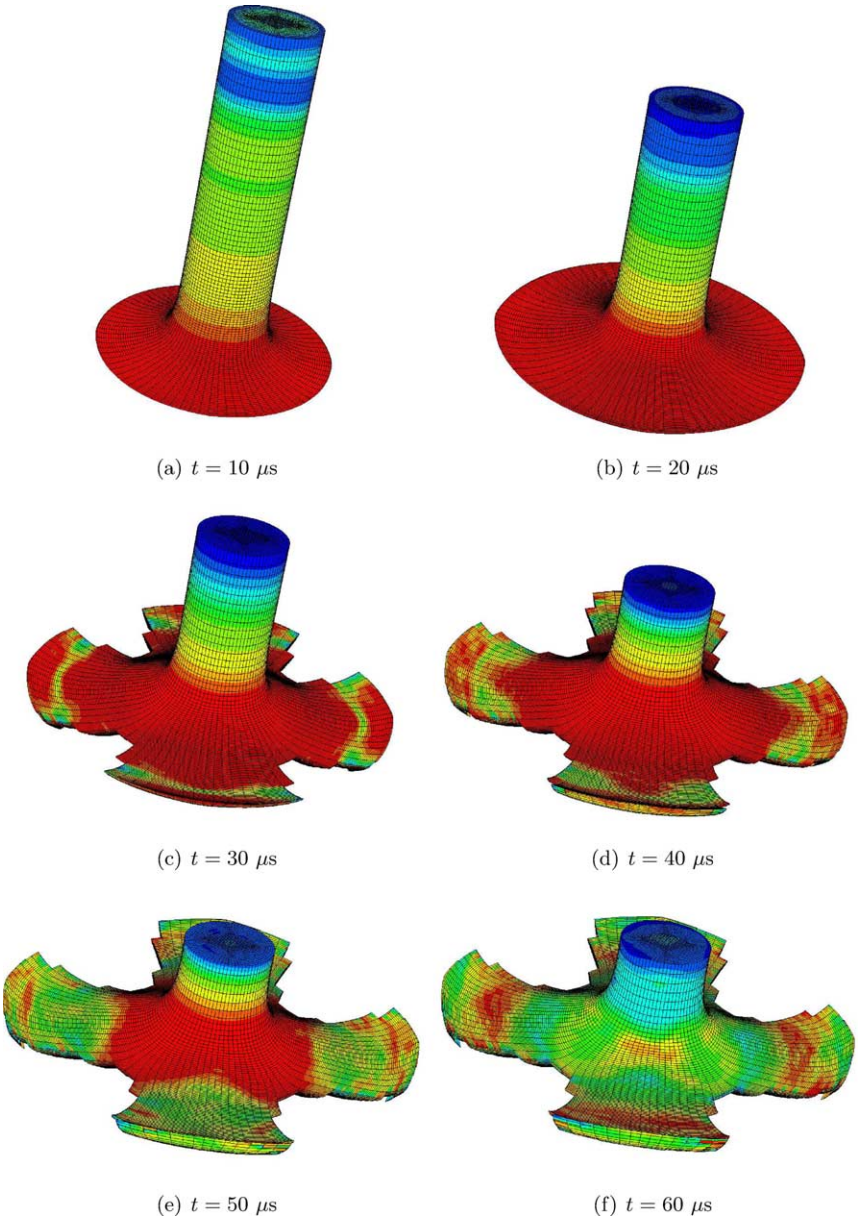

Fig. 12. Petalling process of the Weldox 460 E steel projectile at $V_0 = 600\,\mathrm{m/s}$.

As shown in Fig. 13, the stress triaxiality at this point is always positive except in the very beginning. Its value is very close to 1/3 during the whole impact process, which indicates the predominantly uniaxial stress state in this point. In actuality, the periphery of the front surface moves upward in the mushrooming process and is disconnected from the rigid wall immediately after impact. Hence, the tensile hoop stress is only an acting stress component at the periphery of the front surface.

In this case, the outer edge of the front surface of the cylinder gradually curls up during the impact process. The curling of the front surface is not evident in the preceding cases. Here, four petals are generated.

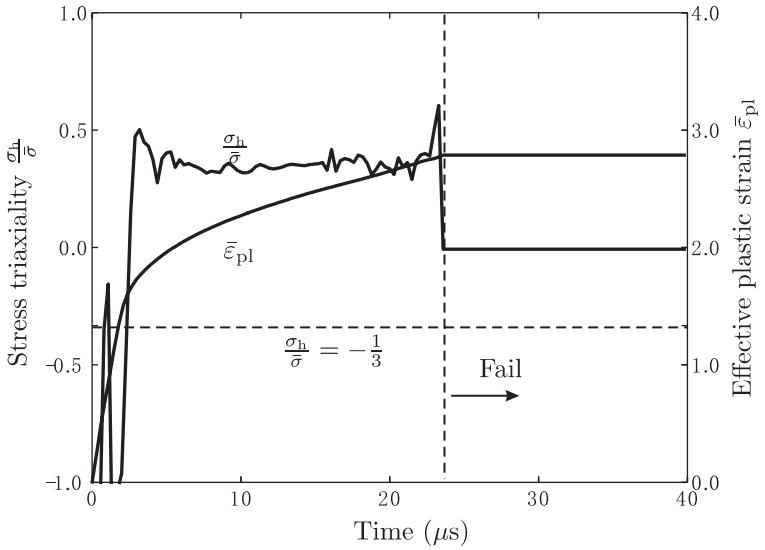

Fig. 13. History of the effective plastic strain and the stress triaxiality of a point at the outer edge of the front surface for the Weldox 460 E steel projectile at $V_0 = 600\,\text{m/s}$.

The number of the petal probably depends on the impact velocity, the ductility of the material, and the geometrical size of the projectile, which needs to be further investigated.

3.4. Shear cracking

The third possible fracture mode in the Taylor test is identified as shear cracking. Consider the cylinder made of 2024-T351 aluminum alloy fired at $V_0 = 240\,\text{m/s}$. The Bao–Wierzbicki's fracture locus was defined in the simulation.

As the front part of the projectile near the rigid wall bulges out, several cracks initiate at the periphery of the front surface, and grow spirally on the lateral surface of the projectile (see Fig. 14). This failure pattern is similar to that in quasi-static upsetting tests where a shear crack is formed near the equator of a specimen

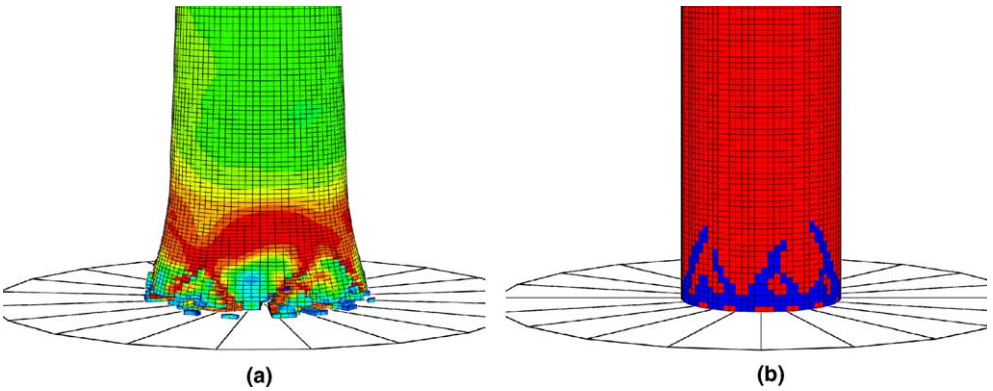

Fig. 14. Shear cracks on the lateral surface of the projectile at $V_0 = 240\,\text{m/s}$. (a) Spiral shear cracks on the deformed projectile. (b) Spiral shear cracks mapped back on the undeformed shape represented by the dark (blue) elements.

due to barrelling and resulting tensile hoop stress (The front surface of the projectile in the Taylor test is equivalent to the equator plane of the cylinder in the upsetting test.).

A typical point at the periphery of the front surface, where a crack initiates, is selected to illustrate the history of both the stress triaxiality and the effective plastic strain. As seen from Fig. 15, a large part of the stress triaxiality during the impact process falls in the range from -0.3 to 0.0, which are typical values in upsetting tests (Bao and Wierzbicki, 2004). Due to dominant compression, there is friction between the newly formed crack surfaces, which destroys microcharacteristics on the crack surfaces, and makes the crack surface more smoother in Mode II than in Mode I.

The present numerical prediction is consistent with the experimental results by Couque (1998) in which the symmetric Taylor tests were conducted and several 45° shear cracks were observed on the lateral surface of both cylinders (Fig. 16). The cylinders were made of swaged tungsten alloy of static elongation of 10%. No shear cracking is observed for the projectile made of Weldox 460 E steel in numerical simulations, which is more ductile than 2024-T351 aluminum alloy and swaged tungsten alloy. Correspondingly, in upsetting

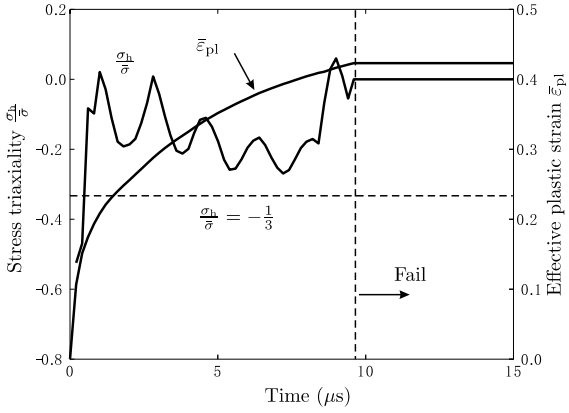

Fig. 15. History of the effective plastic strain and the stress triaxiality at a point on the edge of the front surface of the 2024-T351 aluminum alloy projectile at $V_0 = 240\,\mathrm{m/s}$.

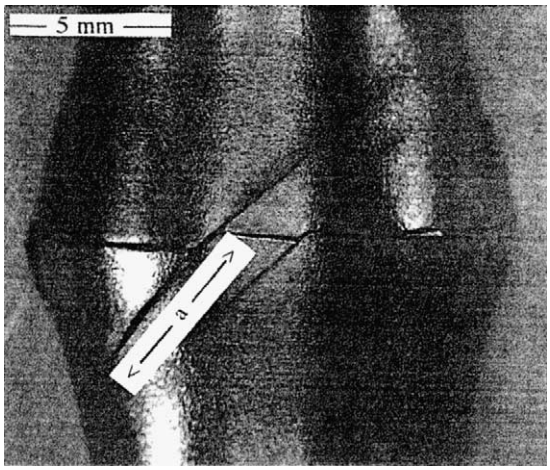

Fig. 16. Shear cracking on the lateral surface of two swaged tungsten alloy cylinders in the symmetric Taylor test (Couque, 1998).

tests a ductile short cylinder can be pressed to a large extent without any evidence of shear cracks on the lateral surface. Hence, shear cracking would more likely take place in a less ductile projectile while tensile petalling in a more ductile cylinder. At a higher impact velocity, shear cracks initiated on the lateral surface would grow toward the interior of the projectile, and eventually the front region of the projectile would break into several parts.

4. Effects of fracture criteria for negative stress triaxialities

Most of ductile fracture criteria studied in the literature were calibrated on basis of tensile tests on notched and smooth axisymmetric specimens. In real situations, a structural component may be subjected to not only tension but also shear and compression. A question naturally arises whether one would be able to use a fracture locus obtained from tensile tests alone to predict fracture in a case where compression is dominant such as the Taylor test. In this section studied are effects of the type of ductile fracture criteria on the fracture response.

Fig. 17 shows the final fracture patterns of the Weldox 460 E steel projectile at $V_0 = 600\,\mathrm{m/s}$ among four combinations of fracture options. The fracture criteria with and without the cut-off value shown in Fig. 6 were implemented in the calculations, respectively. At the same time, it is assumed that either the failed element completely lose the load-carrying capability or are still able to resist pressure. Hence, there is a total of

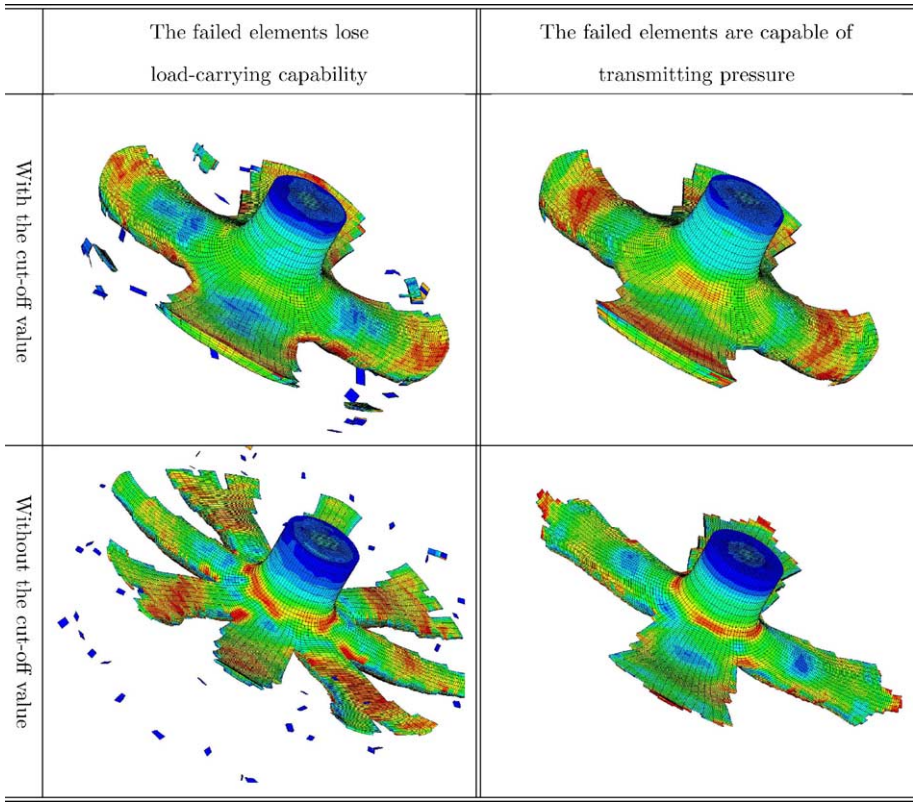

Fig. 17. Comparison of failure patterns of the Weldox 460 E steel projectile at $V_0 = 600\,\mathrm{m/s}$ among various fracture options.

four combinations. All the failed elements have been removed to show the generated cracks and fragments. It appears that the fracture locus without the cut-off value predicts more petal numbers and/or longer crack length than that with the cut-off value. In a way fracture models that disregard the effect of the cut-off value make materials to be artificially brittle. A number of fragments escape from the projectile in the case where the failed elements are assumed to completely lose the load-carrying capability, see the graphs on the left hand side of Fig. 17. These fracture patterns probably are unrealistic, since the cylinder is made of a much ductile material.

The effect of the cut-off value on the predicted failure pattern of the cylinder becomes evident when comparing the failed region among these four cases (Fig. 18). Note, that the central part of the cylinder is predominantly under compression. The predicted size of the failed region is much smaller in the cases with the cut-off value than without the cut-off value. In reality, failed materials would be still attached to specimens. The size of the failed region may be determined by checking metallurgical microstructures of post-test specimens.

Beside a different fracture pattern, also the time history of the velocity of the rear surface can be studied to distinguish between various types of fracture criteria. Immediately upon impact, an axial elastic stress wave is generated followed by a plastic stress wave travelling at a much lower velocity. As the axial elastic stress wave propagates back and forth from the rear surface to the elastic–plastic boundary, the velocity of

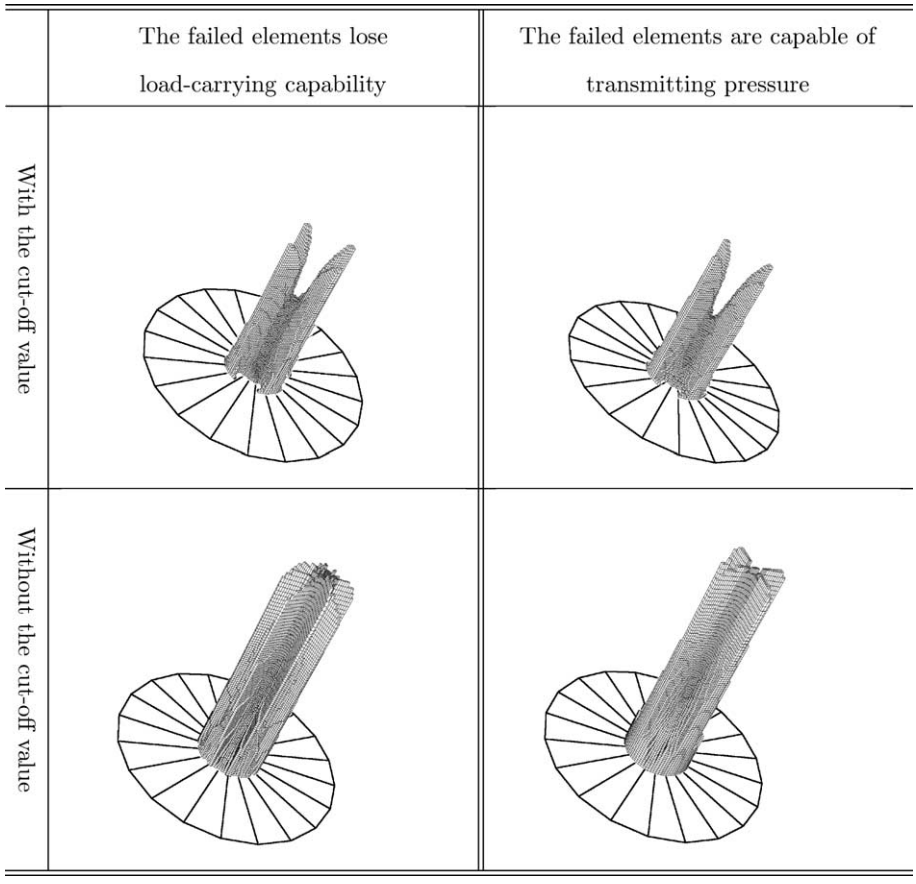

Fig. 18. Comparison of the size of the failed region in the undeformed form for the Weldox 460 E steel projectile at $V_0 = 600\,\mathrm{m/s}$.

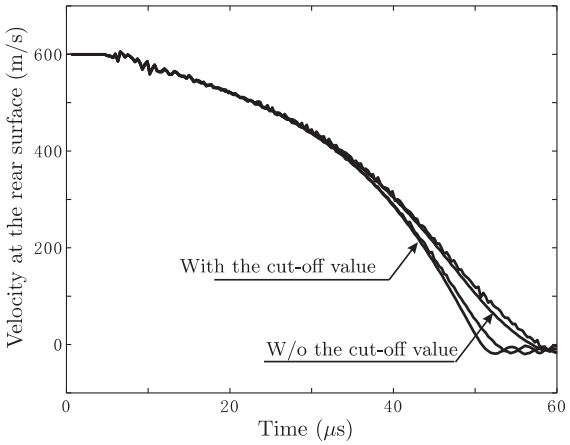

Fig. 19. Comparison of the velocity history of the rear surface of the Weldox 460 E steel projectile at $V_0 = 600\,\mathrm{m/s}$ among four cases.

the rear surface decreases in a step-wise way. The movement of the rear surface can be measured using the so-called VISAR (velocity interferometer system for any reflector) technique. The measured time history of the velocity of the rear surface can be used to verify material constitutive models by comparing with numerical results, e.g. as proposed by Rohr et al. (2003). However, tracking the velocity history appears not to be very useful to verify the fracture criterion if the cylinder fails by petalling in the Taylor test. As shown in Fig. 19, there is not much difference in the calculated velocity history of the rear surface among four cases. However, this observation is not true for shear cracking. As we can see from Fig. 20 that the JC's and BW's fracture loci give different velocity–time history for the 2024-T351 aluminum alloy where a projectile fails by shear cracking.

The effects of the type of ductile fracture criteria on the failure response of the 2024-T351 aluminum alloy were also investigated. Fig. 21 shows the final fracture patterns of the cylinder at $V_0 = 240\,\mathrm{m/s}$ using the JC's and BW's fracture loci, respectively. In contrast to the BW's fracture locus, the JC's fracture criterion does not capture shear cracking on the lateral surface of the cylinder. Elements in the front part of the

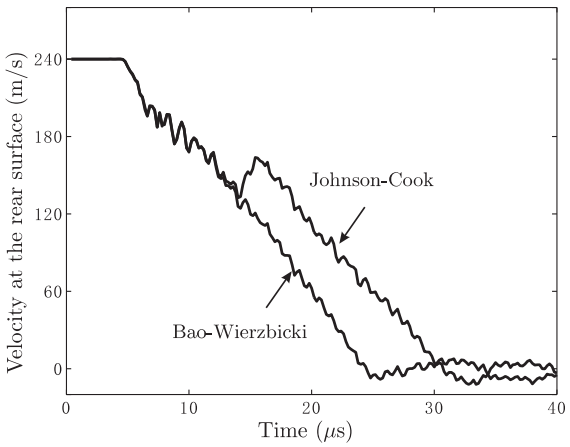

Fig. 20. Comparison of the velocity history of the rear surface of the 2024-T351 aluminum alloy projectile at $V_0 = 240\,\mathrm{m/s}$ between Johnson–Cook's and Bao–Wierzbicki's fracture loci.

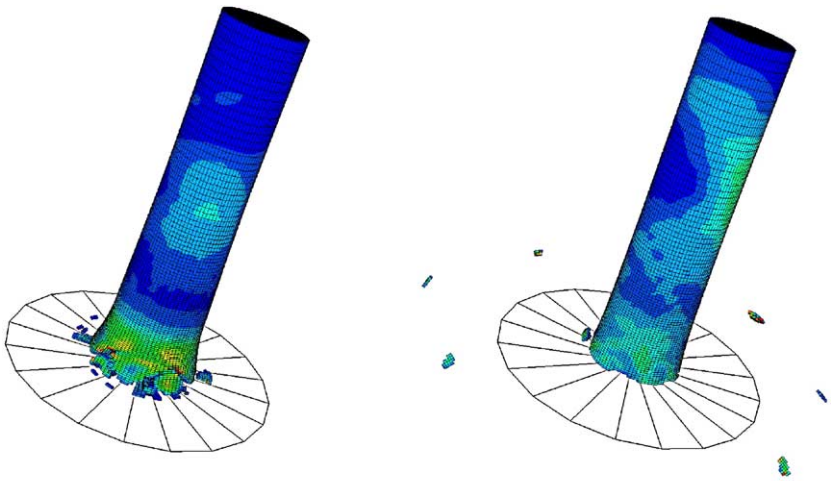

Fig. 21. Comparison of the final fracture patterns for the 2024-T351 aluminum alloy projectile at $V_0 = 240\,\mathrm{m/s}$. It is assumed in both cases that the failed elements are still capable of transmitting pressure. The failed elements have been removed to show generated cracks.

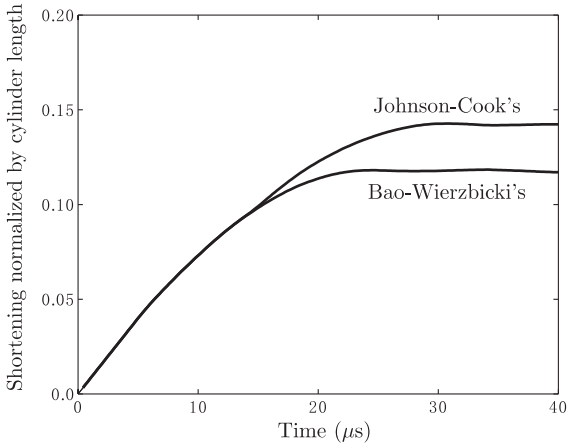

Fig. 22. Comparison of shortening history of the 2024-T351 aluminum alloy projectile at $V_0 = 240\,\mathrm{m/s}$ based on the JC's and BW's fracture loci, respectively.

cylinder are artificially eroded layer by layer until the impact velocity is decreased to a certain level, which leads to a shorter final length of the cylinder (see Fig. 22). This seems unrealistic. Tests are being planned to verify the accuracy of the above numerical simulations.

5. Concluding remarks

In this paper, the mechanisms of fracture in the Taylor test were investigated numerically on basis of the newly developed Bao–Wierzbicki's ductile fracture locus. Three possible fracture modes were successfully

recreated: confined fracture inside the cylinder, petalling of the front surface, and shear cracking on the lateral surface, all of which are consistent with experimental observations presented in the open literature. Petalling would more likely take place in a more ductile projectile fired at a higher velocity while shear cracking in a less ductile material. The effect of the type of the fracture locus was also studied by comparing the fracture process between the cases with and without the cut-off value. It appears that the fracture locus with the cut-off value gives more realistic results.

The initial impact velocity considered in the present paper ranges from 240 m/s to 600 m/s. In this sub-ordnance range, distinct fracture macro-modes have been observed. If the impact velocity is further increased, the cylinder may fail by adiabatic shear banding or fragmentation, which is beyond the scope of the present paper.

In the present simulation, the impacted wall is assumed to be rigid. In reality, the struck body is, more or less, deformable or breakable. Numerical simulation of interactive failure of a cylinder impact against a deformable circular plate is under way. In addition, tests are being planned at Ernest Mach Institute in Germany to validate the present numerical findings experimentally.

References

Addessio, F.L., Johnson, J.N., Maudlin, P.J., 1993. The effect of void growth on Taylor cylinder impact experiments. Journal of Applied Physics 73 (11), 7288–7297.

Bai, Y., Dodd, B., 1992. Adiabatic Shear Localization: Occurrence, Theories and Applications. Pergamon Press, New York.

Bao, Y., Wierzbicki, T., 2004. On fracture locus in the equivalent strain and stress triaxiality space. International Journal of Mechanical Sciences 46 (1), 81–98.

Bao, Y., Lee, Y., Wierzbicki, T. Evaluation and calibration of seven fracture models. International Journal of Mechanical Sciences, submitted.

Børvik, T., Hopperstad, O.S., Berstad, T., Langseth, M., 2001a. Numerical simulation of plugging failure in ballistic penetration. International Journal of Solids and Structures 38 (34–35), 6241–6264.

Børvik, T., Hopperstad, O.S., Berstad, T., Langseth, M.L., 2001b. A computational model of viscoplasticity and ductile damage for impact and penetration. European Journal of Mechanics: A/Solids 20, 685–712.

Børvik, T., Hopperstad, O.S., Berstad, T., Langseth, M., 2002. Perforation of 12 mm thick steel plates by 20 mm diameter projectiles with flat, hemispherical and conical noses part II: Numerical simulations. International Journal of Impact Engineering 27 (1), 37–64.

Børvik, T., Hopperstad, O.S., Berstad, T., 2003. On the influence of stress triaxiality and strain rate on the behaviour of a structural steel. Part II: Numerical study. European Journal of Mechanics A/Solids 22, 15–23.

Couque, H., 1998. On the use of the symmetric Taylor test to evaluate dynamic ductile compression fracture properties of metals. In: Proceedings of the 5th International Conference on Structures Under Shock and Impact. Computational Mechanics Inc, Billerica, MA, USA.

Grady, D.E., Kipp, M.E., 1989. Fragmentation of solids under dynamic loading. In: Wierzbicki, T., Jones, N. (Eds.), Structural Failure. John Wiley & Sons, New York, pp. 1–40 (Chapter 1).

Gurson, A.L., 1975. Plastic flow and fracture behavior of ductile materials incorporating void nucleation, growth and interaction, PhD thesis, Brown University.

Hopperstad, O.S., Børvik, T., Langseth, M., Labibes, K., Albertini, C., 2003. On the influence of stress triaxiality and strain rate on the behaviour of a structural steel Part I: Experiments. European Journal of Mechanics A/Solids 22, 1–13.

Johnson, G.R., Cook, W.H., 1983. A constitutive model and data for metals subjected to large strains, high strain rates and high temperatures. In: Proceedings of the Seventh International Symposium on Ballistics, Hague, Netherlands.

Johnson, G.R., Cook, W.H., 1985. Fracture characteristics of three metals subjected to various strains, strain rates, temperatures and pressures. Engineering Fracture Mechanics 21 (1), 31–48.

Johnson, G.R., Holmquist, T.J., 1988. Evaluation of cylinder-impact test data for constitutive model constants. Journal of Applied Physics 64 (8), 3901–3910.

McClintock, F.A., 1968. A criterion for ductile fracture by the growth of holes. Journal of Applied Mechanics 35, 363–371.

Rice, J.R., Tracey, D.M., 1969. On the ductile enlargement of voids in triaxial stress fields. Journal of the Mechanics and Physics of Solids 17, 201–217.

Rohr, L., Nahme, H., Thoma, K., 2003. A modified Taylor-test in combination with numerical simulations—a new approach for the determination of model parameters under dynamic loads. Journal De Physique IV France 110, 513–518.

Taylor, G.L., 1948. The use of flat-ended projectiles for determining dynamic yield stress. I. Theoretical considerations. In: Proceedings of the Royal Society of London Series A. Mathematical and Physical Sciences 194 (1308), 289–299.

Teng, X., Wierzbicki, T., 2004. Effects of fracture criteria on high velocity perforation of thin beams. International Journal of Computational Methods 1 (1), 171–200.

Walley, S., 2003. Bibliographies on dynamic topics. Available from: http://www.dymat.org.

Woodward, R.L., O'Donnell, R.G., Flockhart, C.J., 1992. Failure mechanisms in impacting penetrators. Journal of Materials Science 27, 6411–6416.

Worswick, M.J., Pick, R.J., 1995. Void growth and coalescence during high-velocity impact. Mechanics of Materials 19, 293–309.